



Heterostructured Nanocomposites of Ag Doped Fe_3O_4 Embedded in ZnO for Antibacterial Applications and Catalytic Conversion of Hazardous Wastes

Avis Tresa Babu¹ · Meera Sebastian¹ · O. Manaf² · Rosy Antony¹

Received: 27 August 2019 / Accepted: 22 October 2019 / Published online: 25 October 2019
© Springer Science+Business Media, LLC, part of Springer Nature 2019

Abstract

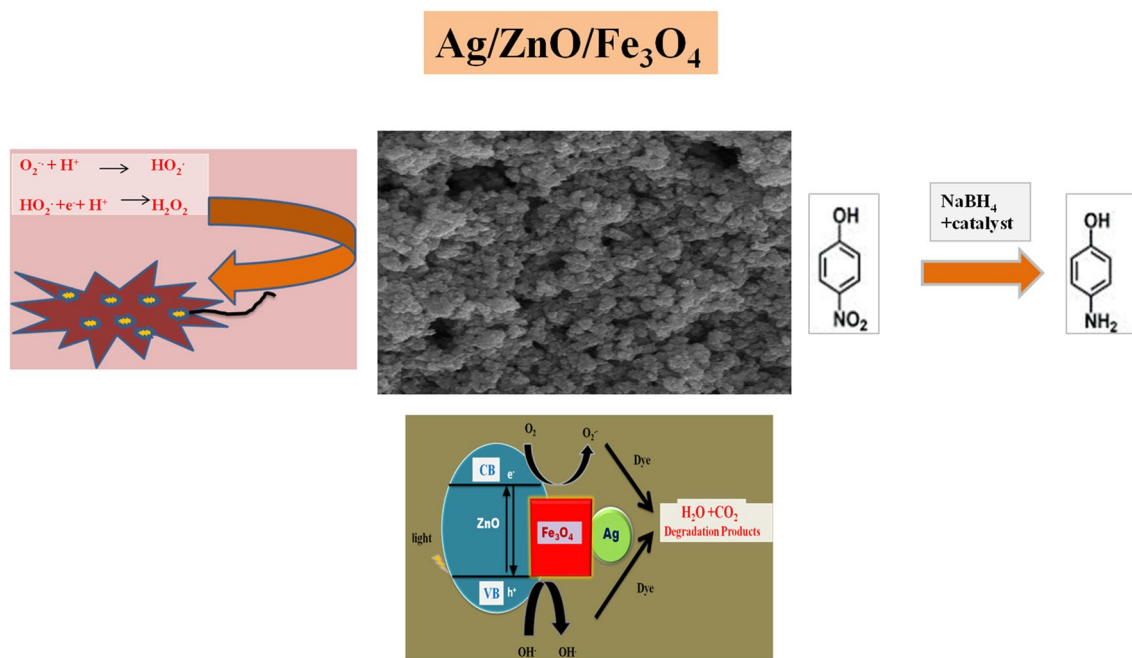
Heterostructured ternary nanocomposites of silver doped magnetites with ZnO (Z), namely Ag/ZnO (AZ), Ag/ Fe_3O_4 (AF), ZnO/ Fe_3O_4 (ZF) and Ag/ZnO/ Fe_3O_4 (AZF) were synthesized. X-ray diffraction studies indicated the formation of wurtzite hexagonal phase for ZnO, cubic structure for Fe_3O_4 and FCC structure for silver nanocomposites. Field emission scanning electron microscopy revealed the uniform distribution of granules of AZF. Fourier transform infrared spectroscopic studies confirmed the presence of M–O bonds. The ultra violet-visible diffuse reflectance spectroscopy and photoluminescence studies indicated the higher photo degradation activity of silver doped nanocomposites. Thermogravimetric analysis point towards the enhanced thermal stability of doped and coupled nanocomposites. Hydrogenation of 4-nitrophenol to 4-aminophenol showed that AZ, AF & AZF completed the reaction within 3, 4 & 2 min respectively while Z and ZF are ineffective. The photo catalytic activity of the nano composites was investigated by studying the degradation of malachite green (MG) & methylene blue (MB) under UV irradiation. Hetero structured and Ag doped nano composites exhibited better degradation efficiency of MG & MB. Using well diffusion method antibacterial activity of the as-prepared nanoparticles was tested against gram-positive bacteria *Staphylococcus aureus* and gram negative bacteria *Escherichia coli*. AF & AZF nanocomposites exhibited strong antibacterial activity with greater inhibition zones due to the synergistic effect of silver and magnetite nanoparticles.

✉ Rosy Antony
drrosy.antony3@gmail.com

¹ Post Graduate and Research Department of Chemistry,
Nirmalagiri College, Kannur, Kerala 670701, India

² Department of Chemistry, National Institute of Technology
Calicut, Kozhikode, India

Graphic Abstract



Keywords Heterostructured nanocomposites · Ag/ZnO magnetites · Antibacterial agent · Photocatalysis · Catalytic reduction

1 Introduction

Heterogeneous nanocomposites are attractive since they possess multifunctional properties for magnetic, electronic, optical, catalytic and photocatalytic applications [1–3]. Metal oxides immobilized on solid matrix have weaker photocatalytic activity owing to the significant decrease of the solid to liquid contact areas. To overcome this problem, magnetic components can be incorporated suitably into semiconductor metal oxide which can be retrieved effectively by simply applying suitable magnetic fields. The synergistic interactions between metal nanoparticles and semiconductor/magnetic metal oxide supports contribute to the enhanced properties [4]. The high band gap energy of ZnO necessitates the irradiation of UV for photocatalysis and also high electron–hole recombination rate reduces its catalytic efficiency [5, 6]. Noble metals, such as Ag, Au, Pt when used as dopants have proved to increase the photocatalytic efficiency of semiconductors [7]. It has been reported that ZnO-based ternary nanocomposites have superiority over binary composites. Combining the advantages of magnetic materials and noble metal to fabricate a promising catalyst opens new possibilities for the achievement of desirable catalytic activity and effective magnetic separability.

Fe₃O₄ nanoparticles possess better optical, electrical, magnetic, and thermal properties and are widely used in catalysis, ferrofluids, biomedical and data storage [8]. Their insolubility, super paramagnetism and efficient magnetic response in an external magnetic field enable the isolation of catalysts from reaction mixture. It would be beneficial to fabricate Fe₃O₄ nanoclusters as core in semiconductor embedded nanocomposites which shields Fe₃O₄ from exposure to air, moisture and the pollutants [9]. ZnO can be an appropriate shell material with large surface area and pore volumes for absorption of pollutant molecules which can protect Fe₃O₄ core from the exciting radiation [10].

Organic pollutants are becoming a major cause of ecological contamination as industrial effluents which include hazardous organic dyes and phenolic compounds [11, 12]. Different methods for waste water treatment include oxidation, filtration, coagulation, adsorption etc. The “Advanced Oxidation Processes (AOPs)” is an innovative field for the effluent treatment. The organic compounds and water pathogens are degraded into CO₂ and water by the highly reactive free radicals OH[•], O₂^{•-} etc. Metal oxide semiconductor materials are efficient heterogeneous photocatalysts and act as AOPs which could mineralize the organic waste without any harmful byproducts [13].

Nitrophenol is a major pollutant in industrial effluents and agricultural wastewater [14]. It can be removed by any of the following techniques such as adsorption [15], photocatalysis, chemical oxidation [16] and electrochemical method [17]. The reduction of 4-nitrophenol (4-NP) using heterogeneous nanocatalysts in the presence of NaBH_4 yields 4-AP. 4-Aminophenol is a useful intermediate in the manufacture of analgesic and antipyretic drugs [18]. 4-AP has been extensively used as anticorrosion agent. It finds applications in photographic developer and hair-dyeing agent [19]. This catalytic reduction offers to be an effective green chemistry technique without causing any secondary pollutants.

Nanosized heterogeneous metal oxides have proved to be effective antibacterial materials due to their large surface area and unique physico—chemical properties [20]. It has been reported that TiO_2 , ZnO, CuO, MgO as well as silver possess antimicrobial properties. Since silver and its compounds have powerful antimicrobial activity over a wide spectrum of pathogens, different medical devices such as urinary catheters, suture rings and packaging material have nanoparticles of silver as an antiseptic agent [21–24]. However, chronic exposure to silver possesses adverse health effects and cause argyrosis and argyria. It has been reported that nanoparticles of silver embedded on magnetic microspheres could be delivered specifically to the infected area by using magnetic fields.

In this work, the mixed metal oxide nanocomposites were prepared by co-precipitation method. To prevent the agglomeration of nanoparticles poly vinyl pyrrolidone (PVP) was used as surfactant. The photocatalytic activity of $\text{Ag/Fe}_3\text{O}_4/\text{ZnO}$ was investigated in comparison with ZnO, Ag/ZnO , $\text{Ag/Fe}_3\text{O}_4$ & $\text{ZnO/Fe}_3\text{O}_4$ in the presence of photo-Fenton catalytic reagent (H_2O_2) against MG and MB. The antimicrobial ability of the heterostructured nanocomposites were studied against *Escherichia coli* (*E. coli*) and *Staphylococcus aureus* (*S. aureus*) by well diffusion assay. The catalytic efficiency of the nanocomposites for the reduction of 4-nitrophenol to 4-aminophenol was studied in presence of NaBH_4 .

2 Materials and Methods

Zinc nitrate, silver nitrate, ferrous sulphate, ethanol, oxalic acid, PVP, 4-nitro phenol, sodium borohydride, methylene blue and malachite green dye were purchased from Merck Chemical Reagent Co. Ltd. India. The bacterial strains used for screening were Gram negative *E. coli* (MTCC 2842) and Gram positive *S. aureus* (MTCC 3160), Stock solutions of MG & MB were prepared by dissolving 400 mg of dye in one liter of water. Millipore water was used for all the experiments.

2.1 Synthesis of ZnO and Ag/ZnO

$\text{Zn}(\text{NO}_3)_2 \cdot 6\text{H}_2\text{O}$ (2.5 mmol) was dissolved in water by the addition of PVP and stirred homogeneously for half an hour. Reaction temperature was maintained at 60 °C. An aqueous solution of NaOH was added to the above solution at a pH of 11–12. The resulting precipitate was collected, filtered, washed and dried at 80 °C for 24 h. The precipitate was calcined at 600 °C for 2 h. Silver doped nanoparticles were also prepared by the above co-precipitation method using nitrates of zinc and silver as precursors.

2.2 Synthesis of Ag/Fe₃O₄

For the preparation of $\text{Ag/Fe}_3\text{O}_4$ nanocomposite 0.7 g (2.5 mmol) of $\text{FeSO}_4 \cdot 7\text{H}_2\text{O}$ and 0.07 g (0.25 mmol) of $\text{Ag}(\text{NO}_3)_2$ were dissolved in water with vigorous stirring to form solution A. 0.63 g of oxalic acid and 0.5 g PVP were dissolved in ethanol with vigorous stirring to form solution B. Solution A was added drop by drop to solution B with continuous stirring. After addition, the stirring was continued for another 5 h and the precipitate obtained was centrifuged, washed thoroughly by ethanol & water and dried at 80 °C for 2 h. The obtained nanocomposite was calcined at 500 °C for 2 h to form $\text{Ag/Fe}_3\text{O}_4$.

2.3 Synthesis of ZnO/Fe₃O₄ and Ag/ZnO/Fe₃O₄

$\text{Fe}_3\text{O}_4/\text{ZnO}$ nanocomposite was synthesized by simple co-precipitation method using $\text{FeSO}_4 \cdot 7\text{H}_2\text{O}$ and $\text{Zn}(\text{NO}_3)_2 \cdot 6\text{H}_2\text{O}$ as salt precursors. PVP was used as structure directing agent. For the preparation of $\text{ZnO/Fe}_3\text{O}_4$ nanocomposites, 0.7 g (2.5 mmol) of $\text{FeSO}_4 \cdot 7\text{H}_2\text{O}$ and 0.43 g (2.5 mmol) of $\text{Zn}(\text{NO}_3)_2 \cdot 6\text{H}_2\text{O}$ were dissolved in water with vigorous stirring to form solution A. 0.63 g of oxalic acid and 0.5 g PVP were dissolved in ethanol with stirring to form solution B. Then solution A was added drop wise to solution B with continuous stirring to form yellowish green precipitate. The stirring was continued for another 5 h and then the precipitate obtained was centrifuged, washed with ethanol & water and dried at 80 °C for 2 h. The obtained nanocomposite was calcined at 500 °C for 2 h to form $\text{ZnO/Fe}_3\text{O}_4$. Silver doped nanocomposites were also prepared by the above co-precipitation method using nitrates of silver as precursor.

2.4 Characterization

The powder X-ray diffraction (XRD) was studied in a 2θ range of 20°–80° using a Rigaku Miniflex-600 with Cu Kα rays at 1.5406 Å with a tube current of 20 mA at 40 kV. A Jasco-v-550 UV/Visible spectrophotometer was used to analysis the UV–Vis diffuse reflectance spectra (DRS).

Thermogravimetric analysis (TGA) was monitored with Netzsch-STA 449-F5 machine, in the temperature range 30–800 °C with heating rate of 10 °C/min under N₂ environment. A Raman spectrum was studied using WITec alpha300RA (WITec GmbH, Ulm, Germany) with the excitation Nd:YAG laser at 532 nm. The FTIR spectra were obtained by FTIR-Spectroscopy (Agilent-Technologies-Cary 630-ATR). The photoluminescence (PL) spectra were recorded via Fluorescence spectrophotometer (Agilent, Cary Eclipse). The surface morphology was analysed by FESEM taken on a FEI Nova NanoSem 450 electron microscope. The corresponding absorbance measurement of reduction of 4-nitrophenol and UV-Visible absorbance of dye solutions were recorded by using an Intech UV-Visible Spectrophotometer-Double beam-2800.

2.5 Photocatalytic Degradation

The photocatalytic efficiency of the nanocomposites was studied using a homemade photoreactor for the degradation of MB & MG (10 mg/L). The aqueous dye solution (100 ml) containing 250 mg photocatalyst was kept in dark to attain adsorption-desorption equilibrium and stirred for 30 min, followed by the addition of 0.1 ml of H₂O₂. UV light source (150 W) was used for irradiation. Aliquots of sample solution were withdrawn at regular intervals of time (5 min) and the absorbance of the supernatant was detected spectrophotometrically. The photodegradation efficiency was calculated as

$$\text{Degradation efficiency(\%)} = \frac{C_0 - C_t}{C_0} \times 100 \quad (1)$$

where, C₀ and C_t are the dye concentrations (mg/L) initially and after time t (in minutes).

2.6 Catalytic Reduction of 4-Nitrophenol

The catalytic efficiency of the nanocomposites was evaluated for the conversion of 4-nitrophenol (4-NP) into 4-aminophenol (4-AP). The aqueous solution of 4-NP (20 mL) and 5.0 mg catalyst were mixed with 250 mM freshly prepared NaBH₄ and kept for stirring. Withdrawing aliquots of the reaction mixture at regular time intervals and quenching it by adding 5 mL of 2 M HCl, the reaction progress was monitored spectrophotometrically. The yellow colour of the 4-NP solution disappeared which indicated the formation of 4-AP at 268 nm.

2.7 Antibacterial Assay

The agar well diffusion technique was used to study the antibacterial activity of nanocomposites against gram-positive

(*S. aureus*) and gram-negative (*E. coli*,) bacteria. Nutrient agar medium was prepared by adding peptone (5.0 g), yeast extract (2.0 g), NaCl (5.0 g) and agar (20 g) in 1 L water. It was sterilized at 130 °C for 40 min in an autoclave under neutral conditions. The nutrient medium was poured into the Muller Hinton agar plate and bacterial lawn was cultured on this. To this, 250 mg of the as prepared nanocomposites were added and incubated at 37 °C for 24 h. The inhibition zone of bacterial growth was measured in mm [25].

3 Results and Discussion

3.1 X-Ray Diffraction Analysis

Figure 1 shows XRD pattern of crystalline phases of as-prepared nanomaterials. It can be inferred that Fe₃O₄, ZnO and Ag nanoparticles have simple cubic, hexagonal wurtzite and face centered cubic crystalline structures with space groups Fd3m, P63mc & Fm3m respectively. The peaks observed at 2θ = 34.50 (0 0 2), 36.22 (1 0 1), 47.46 (1 0 2), 56.54 (1 1 0), 62.96 (1 0 3), 66.44 (2 0 0), 68.08 (1 1 2), 69.16 (2 0 1), 72.12 (0 0 4) and 77.00 (2 0 2) are due to ZnO (JCPDS 01-079-0207). Diffraction peaks at 2θ = 38.06 (1 1 1), 44.32 (2 0 0) and 64.46 (2 2 0) matches well with fcc crystal structure of silver (JCPDS 01-087-0720). The diffraction peaks at 2θ = 31.82 (2 0 0), 35.16 (3 1 1), 42.94 (4 0 0), 53.01 (4 2 2), 56.74 (5 1 1), 62.10 (4 4 0) and 75.73 (6 2 2) corresponds to characteristic peaks of the Fe₃O₄ (JCPDS 75-0033). The diffraction results confirm the presence of nanosized Fe₃O₄, ZnO and Ag in Z, AZ, FZ, AF and AZF nanocomposites.

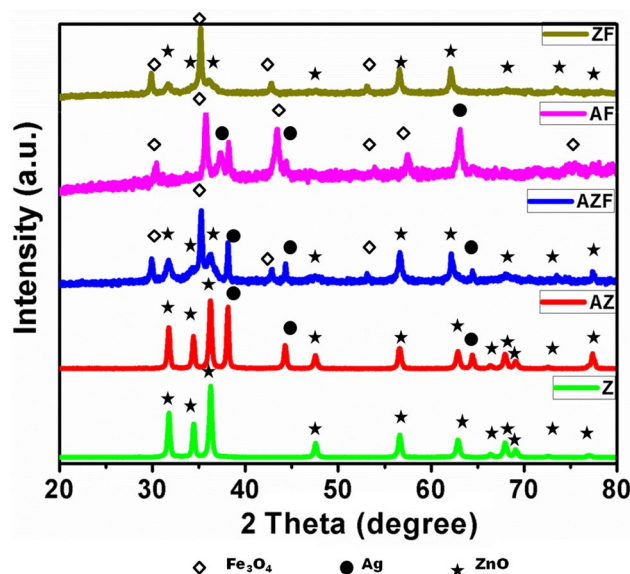


Fig. 1 XRD patterns of Z, AZ, AF, ZF & AZF nanomaterials

By applying Scherrer's formula, the crystallite sizes of the samples were calculated

$$D = \frac{k\lambda}{\beta \cos\theta} \quad (2)$$

where $k=0.94$ is the shape factor, d = average particle size, β is full width at half maxima (FWHM), θ is the Bragg angle, $\lambda=1.541 \text{ \AA}$ is the wavelength of Cu-K radiation. The average size of Z, AZ, ZF, AF and AZF metal oxides were found to be 30.67, 30.31, 75.90, 36.12 and 34.99 nm respectively.

3.2 Fourier Transform Infrared Spectroscopy

The FTIR spectra of the nanomaterials are shown in Fig. 2. IR bands in the region $400\text{--}1000 \text{ cm}^{-1}$ might be due to the M–O and O–M–O bonds. The broad absorption band at $3000\text{--}3500 \text{ cm}^{-1}$ is ascribed to the O–H stretching vibration of the hydroxyl group of water present at the surface of the nanoparticles [26, 27]. The peak at 1625 cm^{-1} is attributed to H–O–H bending vibration of water [28]. The peak located at 2345 cm^{-1} and 1384 cm^{-1} might be due to CO_2 [29]. The other peaks may be due to intramolecular hydrogen bonds [30].

3.3 UV–Visible Diffuse Reflectance Spectroscopy

The UV–Visible diffuse reflectance spectra of Z, AZ, ZF, AF and AZF nanocomposites are given in Fig. 3a–e. Z absorb only in the UV region where as the absorption edge of AZ, AF, ZF and AZF are more extended to visible region. The absorption of AZF, AZ, ZF & AF nanocomposites are higher than that of pristine ZnO as Ag can accept the electrons

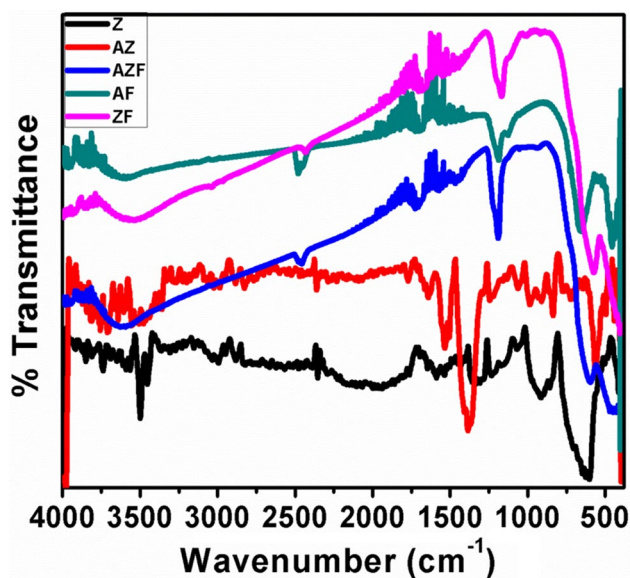


Fig. 2 FTIR spectra of Z, AZ, AF, ZF & AZF nanomaterials

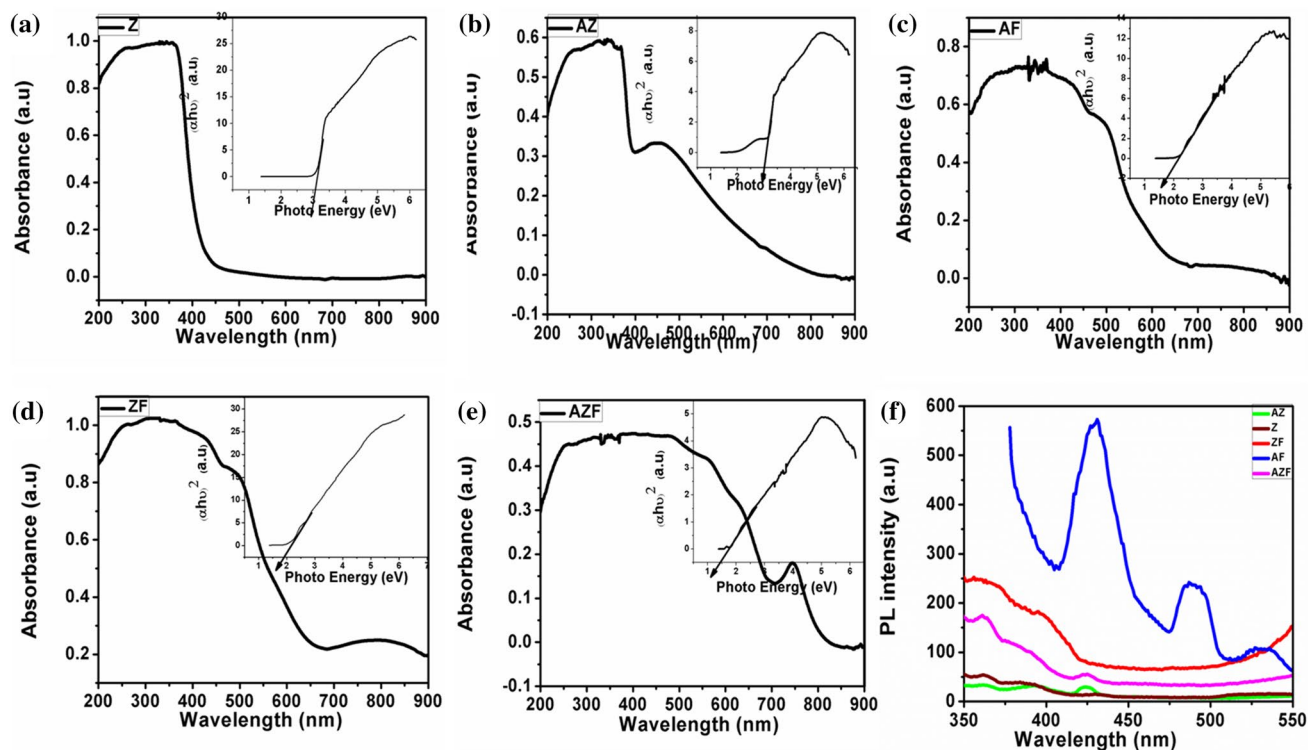


Fig. 3 UV–Visible DRS spectrum (inset: Tauc plot) of a Z, b AZ, c AF, d ZF e AZF and f PL spectra

readily from the radiation. The surface plasmon band of Ag nanoparticles is observed as a new symmetric peak in the wavelength region of 430–470 nm [31, 32]. This accounts for the excellent photo activity of silver doped nanocomposites than ZnO. In the case of AZF, the synergistic affect of ternary composite shifts the absorption band up to 700 nm which is much wider than others. The photocatalytic efficiency of silver doped nanocomposites depends on the surface plasmon resonance of Ag particles. The electron transition from valence band to the conduction band of ZnO causes its intrinsic band-gap (~3.1 eV) absorption which is responsible for the electronic band-edge position at 370 nm in ZnO coupled nanocomposites.

The band gap energy (E_g) of ternary nanocomposites can be estimated from tau plot (inset in Fig. 2) of $(\alpha h\nu)^2$ versus photo energy ($h\nu$), using the following equation [33]:

$$\alpha h\nu = A(h\nu - E_g)^{1/2} \quad (3)$$

where α , ν , E_g , and A are the absorption coefficient, light frequency, band gap, and a constant, respectively. The band gap energy of Z, AZ, ZF, AF and AZF are 3.1 eV, 3.0 eV, 1.9 eV, 1.7 eV & 1.3 eV respectively.

3.4 Photoluminescence Spectroscopy

The charge separation ability of the nanocomposites was determined by using emission spectra [Fig. 3f]. The emission spectrum of AZF shows peaks at 355–385 nm, 396 nm, 423 nm and 517 nm which indicate the electron transition of ZnO nanoparticles present in the composite. The near band edge emission (NBE) of ZnO can be seen at 355–385 nm caused by excitation annihilations which is an indicator of nanosized particles [34]. The peak at 396 nm is due to electron transition from zinc interstitial (Zni) sites to the valence band [35]. The transition of electrons from conduction band to the oxygen interstitial (Oi) sites results in a peak around 423 nm [31]. The weak green emission at around 517 nm, can be due to the charge transfer at the surface defects. Thus the ZnO nanoparticles may have surface defects such as

oxygen vacancies, zinc vacancies, zinc interstitials or oxygen interstitials in the composites [34, 36, 37]. Ag nanoparticles present in the nanocomposite retard the recombination of electrons and holes. The electron trapping occurs from the Fermi energy level of ZnO nanoparticles to that of Ag present in the composite. The degradation efficiency increases by the surface plasma resonance (SPR) also. At the interface of ZnO and Fe_3O_4 , another mode of electron trapping can happen [38]. The reduction of Fe^{3+} ions to Fe^{2+} ions utilize the electrons from the Fermi energy level of ZnO and thus decrease the rate of electron–hole recombination. The photocatalytic efficiency of the ternary nanocomposite enhances by these electron trapping mechanisms.

3.5 Raman Spectroscopy

Figure 4a shows the Raman spectra of the nano metal oxides. The symmetric stretch of oxygen atoms of the Fe–O bonds present in Fe_3O_4 microspheres gives rise to an intense peak around 680 cm^{-1} [39]. The peak at 302 cm^{-1} is characteristic of magnetite. The two weak peaks at 332 and 1095 cm^{-1} can be attributed to the presence of ZnO nanoparticles in the composites [40].

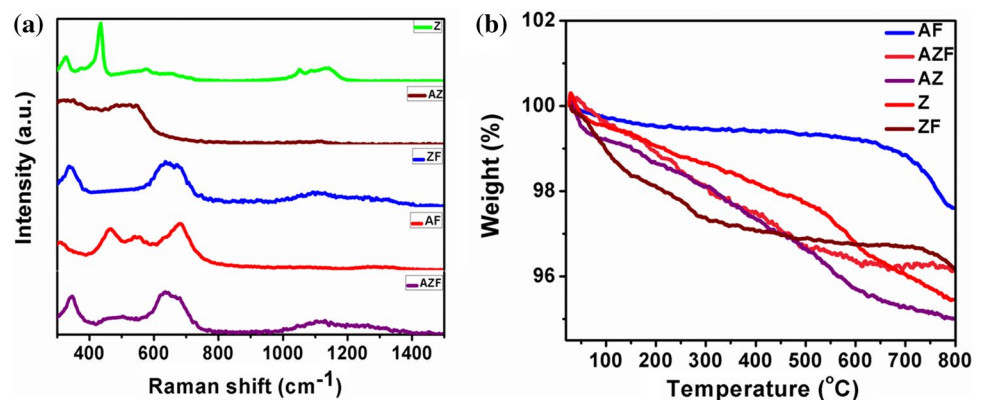
3.6 Thermogravimetric Analysis

The thermograms of the nanoparticles are presented in Fig. 4b. The comparative evaluation of the thermal stability of silver doped ferrites and ZnO nano materials showed that initial weight loss near $150\text{ }^\circ\text{C}$ is due to the removal of surface water. The significant weight loss begins at $300\text{ }^\circ\text{C}$ with char yields of 98%, 96.5%, 96.4, 96% and 95.5% for AF, ZF, AZF, Z and AZ respectively.

3.7 FESEM

Figure 5 shows the FESEM images of Z, AZ, ZF, AF & AZF. The surface morphology was analysed and mainly sphere-like shape could be detected from the images.

Fig. 4 a Raman spectra and b TGA of Z, AZ, AF, ZF & AZF nanomaterials



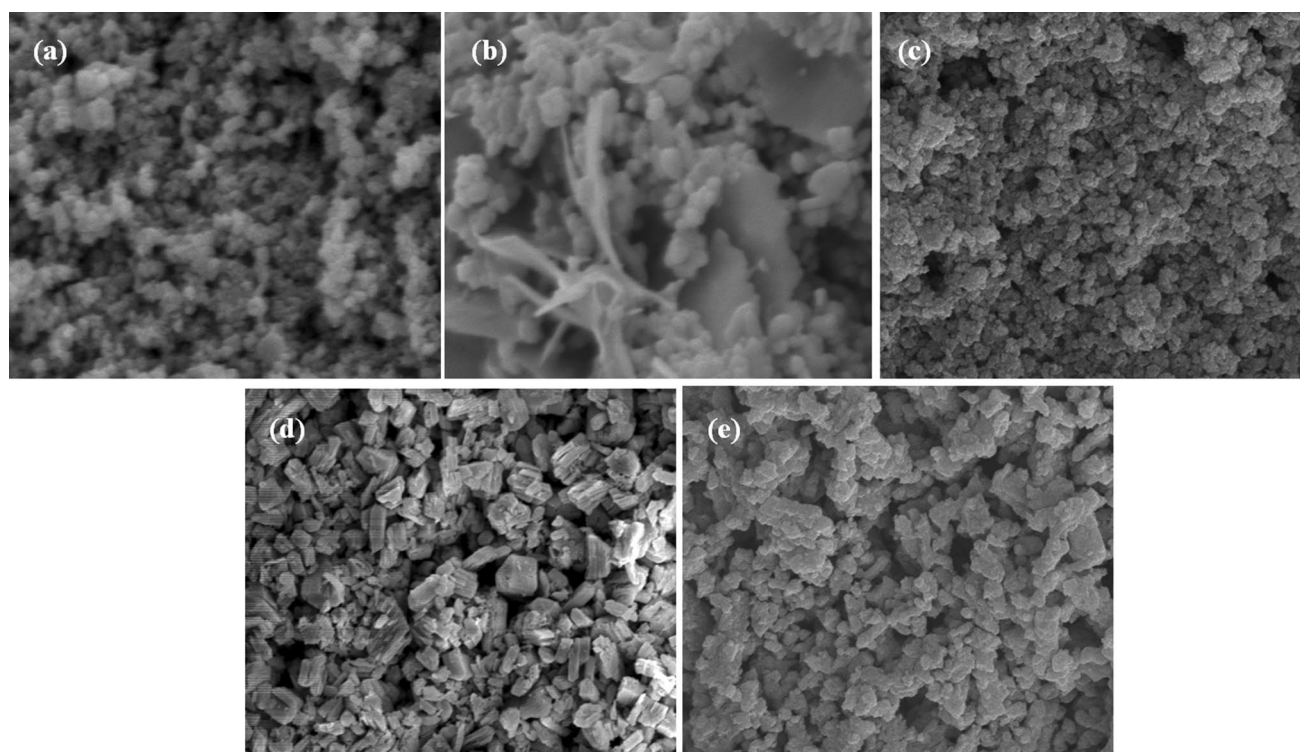


Fig. 5 FESEM micrographs of **a** Z, **b** AZ, **c** AF, **d** ZF and **e** AZF

Figure 5a shows nano beads of ZnO and Fig. 5b displays Ag sheets embedded in spheres of ZnO. Granules of AZF are seen in Fig. 5c with uniform distribution of coupled nano metal oxides. Nano cubes and tubular structures of AF are shown in Fig. 5d. Agglomerated spheres of ZF are presented in Fig. 5e.

3.8 Reduction of 4-Nitrophenol

The catalytic efficiency of nano metal oxides was tested for the reduction of 4-nitrophenol (4-NP) to 4-aminophenol (4-AP). It can be seen that NaBH_4 , when added as the reducing agent took many hours for the completion of the reaction where as in presence of the nano metal oxide catalyst the reduction reaction was instantaneous. The reaction was followed by withdrawing samples at regular intervals of time and the reaction was quenched by the addition of HCl. Figure 6a–d shows the UV–Vis spectra for the reduction reaction. The colour of the solution was changed from yellow to yellowish green due to the formation of 4-nitrophenolate ions and the absorption maximum shifted from 317 to 401 nm. The expected peak of 4-AP at 300 nm showed a blue shift to 268 nm due to the formation of 4-aminophenol hydrochloride. From figures, it can be seen that only silver doped nanocomposites (AZ, AF & AZF) exhibit reduction capacity for the conversion 4-NP to 4-AP when used as hydrogenation catalysts.

The mechanism of the reduction reaction involves the transfer of electron from donor BH_4^- ion to 4-nitrophenol. In presence of silver doped nanocomposites, BH_4^- ion gets adsorbed on the metal surface and electrons discharged from BH_4^- ion through metal oxide to 4-nitrophenol. The hydrogenation is completed by transferring H^+ ions from aqueous medium. In the final step 4-aminophenol is desorbed from the metal surface.

3.9 Photocatalytic Activity

The photocatalytic activities of the as prepared nanocomposites were studied for the degradation of MB and MG dyes. Degradation efficiency of AZ, Z, AZF, ZF & AF for MB and MG was plotted against time and is shown in [Fig. 7a, b]. The degradation efficiency versus time plot shows the relatively higher photocatalytic degradation efficiency of $\text{Fe}_3\text{O}_4/\text{ZnO}/\text{Ag}$, Ag/ZnO , $\text{Ag}/\text{Fe}_3\text{O}_4$ nanocomposites than $\text{Fe}_3\text{O}_4/\text{ZnO}$ and ZnO . It can be seen that the degradation percentage increases with time of exposure and silver doped nanocomposites exhibits higher photodegradation efficiency than the undoped one. The greater photocatalytic degradation after Ag incorporation is due to the involvement of visible light energy and charge transfer. It can be seen that Z and ZF do not show degradation capacity for MB even after 180 min where as AZF degrades MB within 60 min. The greater photocatalytic capacity of the AZF might be attributed to

Fig. 6 Absorption spectra for the reduction of 4-NP by NaBH_4 in aqueous medium in the presence of catalyst **a** (Z & ZF), **b** AZ, **c** AF and **d** AZF

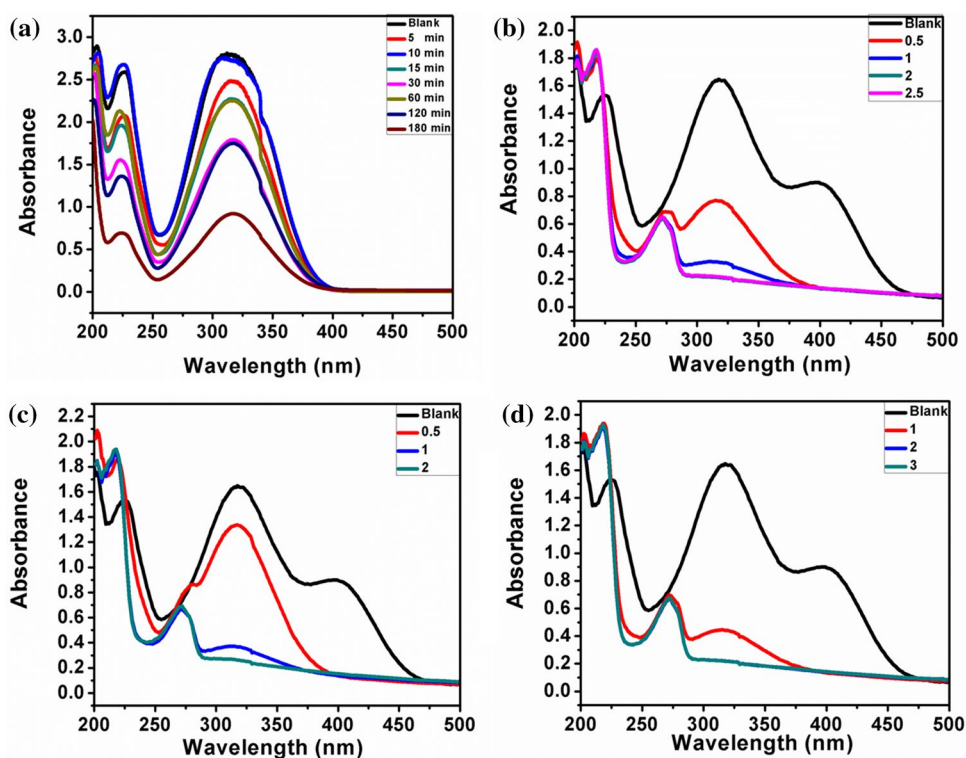
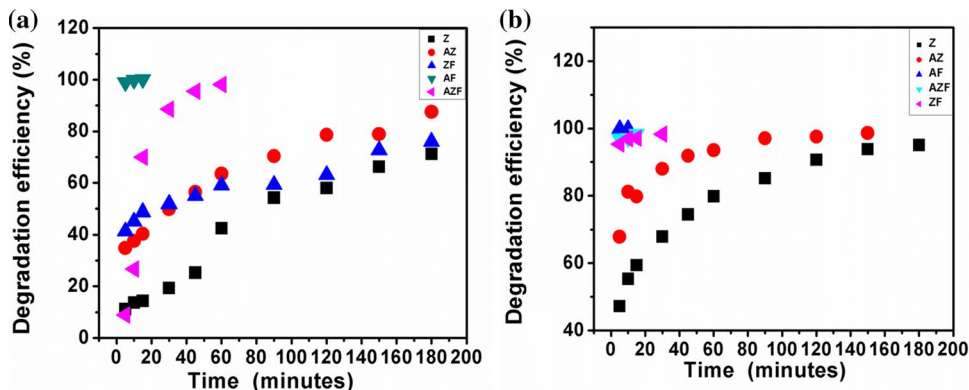


Fig. 7 Degradation capacity of the synthesized nanomaterials for **a** MB and **b** MG

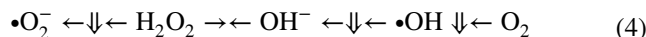


the prevention of recombination of electron–hole pairs. This can be also due to the surface plasmon resonance effect of silver. The degradation studies of MG indicated the superior catalytic activity of Fe_3O_4 microspheres and its composites. The discoloration has been found to be instantaneous for these iron oxide nanocomposites. It has been reported that magnetite not only absorbs light well but also modify the band gap of any material in the nanocomposites thereby enhancing its activity in the visible region [41].

3.10 Photodegradation Mechanism

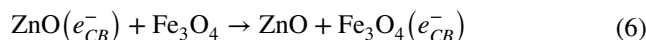
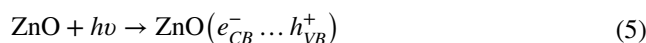
When the energy from visible light radiation becomes greater than the band gap of the semiconductor photocatalyst,

electrons get excited to the conduction band (CB) to produce holes in the valence band (Eqs. 5, 6) [42]. The adsorbed O_2 molecules at catalyst surface combines with the electrons to generate superoxide radical anions (Eq. 7) [43] [Scheme 1]. H_2O_2 present in the medium combines with superoxide radical anions to produce more $(\text{OH}\cdot)$ radicals (Eq. 4).

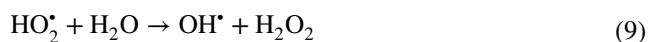
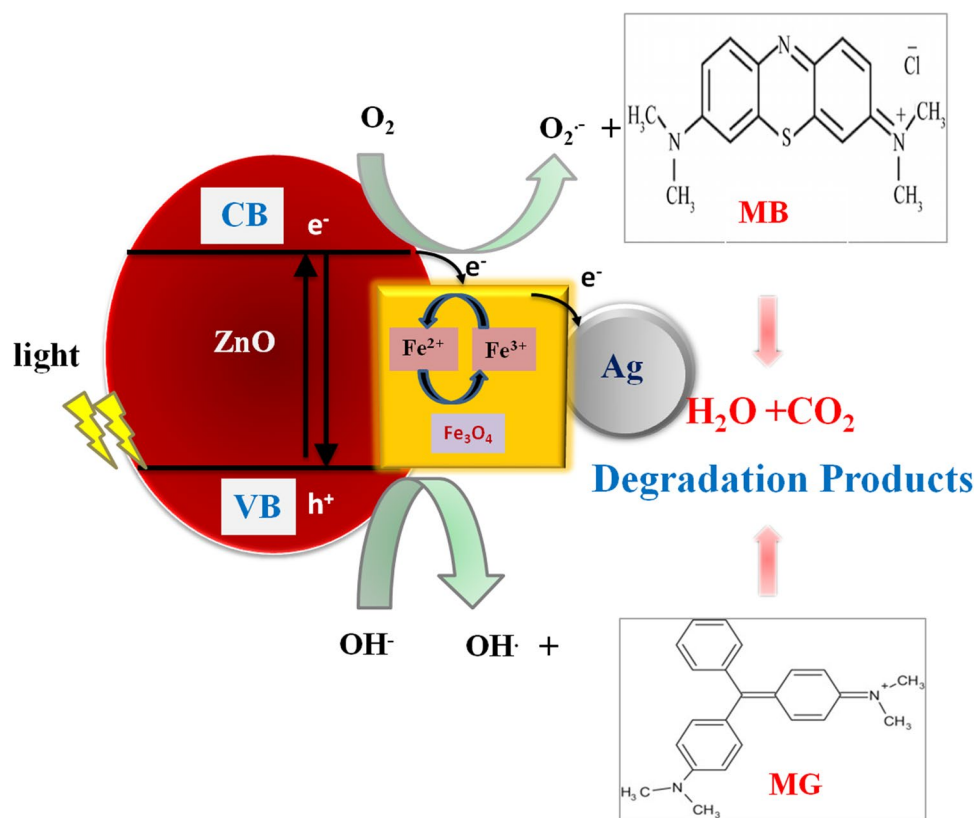


These free radicals react with the dye molecule and degrade it to CO_2 and H_2O .

The degradation mechanism involves:



Scheme 1 Photodegradation process employing Ag/ZnO/Fe₃O₄ nanocomposite



As discussed in section of 3.4 the electrons would have trapped to Fe³⁺ ions and these electrons reduce Fe³⁺ to Fe²⁺ ions. Due to the lower stability of Fe²⁺ ions, they get oxidized immediately by oxygen molecules [32, 38, 44]. The electrons released during this oxidation reaction are used to form O₂^{•-} and the holes generated at the silver nanoparticles form the OH[•].



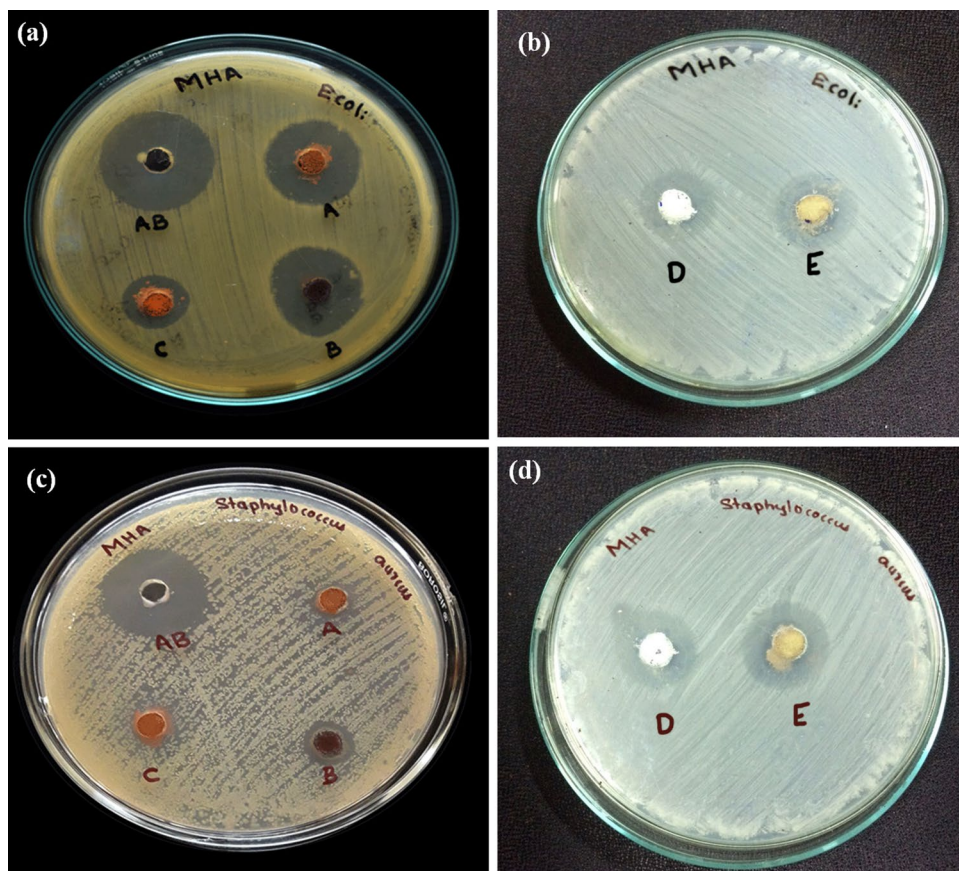
3.11 Antibacterial Activity

The antibacterial activity of the samples Z, AZ, ZF, AF and AZF were tested against *E. coli* (Gram-negative) and *S. aureus* (Gram-positive) by agar well diffusion method

[Fig. 8a–d]. The synergistic effect of antimicrobial performance of silver doped ferrites is indicated from the greater inhibition zones for both *E. coli* and *S. aureus* and shown in Table 1. The gram-negative bacteria are more sensitive than gram-positive bacteria.

The mechanistic pathway of the antibacterial properties involves the attraction between the positively charged metal nanoparticles and the negatively charged microbes attract each other. Thus the microbes get oxidized and are killed. One way of cell cleavage occur due to the reaction between metal ions and the thiol groups present on the bacterial cell surface [45]. Another mechanism of damaging the proteins and DNA in the bacteria might be due to the reactive oxygen species (ROS) generated such as superoxide anion radicals (O₂^{•-}), hydroxyl radicals (•OH) and hydrogen peroxide (H₂O₂) [46]. Kim et al. showed that in ferrites, hydrogen peroxide was generated when Fe²⁺ reacted with oxygen [47]. Subsequently the hydroxyl radicals are produced in the medium which damage the pathogenic bacteria like *S. aureus* & *E. coli*. [48]. In the case of ZnO based nanocomposites, the nanoparticles get accumulated in the outer membrane or cytoplasm of bacterial cells. This activates the release of Zn²⁺ ions followed by cell membrane damage resulting in the death of bacterial cells [49–51].

Fig. 8 Antibacterial activity of synthesized nanomaterials against **a, b** *Escherichia coli* and **c, d** *Staphylococcus aureus* [AB- Streptomycin, A-AF, B-AZF, C-ZF, D-Z & E-AZ]



4 Conclusion

Heterostructured nanocomposites of Ag/ZnO/Fe₃O₄ were synthesized by co-precipitation method. The comparative evaluation of coupled nanocomposites for antibacterial activity, photo degradation efficiency and hydrogenation of aromatics was studied. XRD results showed that the nanocomposite was composed of simple cubic, hexagonal wurtzite and FCC structured Fe₃O₄, ZnO and Ag nanomaterials, respectively. The surface morphology was analysed by FESEM and the nanoparticles were found to have nano

beads, nano cubes and agglomerated structures. Fourier transform infrared spectroscopic studies confirmed the presence of Zn–O and Fe–O bonds below 1000 cm⁻¹. The lower band gap energy and weak PL peaks indicated that the silver doped nanocomposites have higher photo degradation activity. This might be due to defects in the crystal system which can be oxygen vacancies or crystal defects. The oxygen vacancies may trap photo induced charge carriers and suppress their recombination rate. Hydrogenation of 4-nitrophenol showed the instantaneous reduction capacity of silver doped nanocomposites. Coupled nanocomposites containing Fe₃O₄ and Ag exhibited better degradation efficiency of MG & MB. The kinetics of photocatalysis data fit well with pseudo first order model. Thus semiconductor photocatalysis becomes a “green chemistry” approach for degradation of contaminants due to its high mineralization capacity and low toxicity. The antibacterial activity of the as-prepared nanoparticles was tested against gram-positive bacteria *S. aureus* and gram negative bacteria *E. coli*. It was found that coupled nanocomposites of silver doped and magnetite nanoparticles were effective against pathogenic bacteria and possess good catalytic activity for the reduction of 4-nitrophenol.

Table 1 Zone of inhibition of synthesized nanomaterials against *E. coli* & *S. aureus*

Samples	Zone of inhibition (mm)	
	<i>E. coli</i>	<i>S. aureus</i>
ZnO (Z)	17	16
Ag/ZnO (AZ)	20	17
Ag/Fe ₃ O ₄ (AF)	21	12
ZnO/Fe ₃ O ₄ (ZF)	14	10
Ag/ZnO/Fe ₃ O ₄ (AZF)	19	11
Streptomycin (control)	26	25

Acknowledgements The authors are thankful to Dr. Sujith, Associate professor, National Institute of Technology, Calicut, Kerala for

supporting us to carry out the antibacterial work successfully. This research did not receive any specific grant from funding agencies in the public, commercial, or not-for-profit sectors.

References

1. S.H. Jeong, S.Y. Yeo, S.C. Yi, The effect of filler particle size on the antibacterial properties of compounded polymer/silver fibers. *J. Mater. Sci.* **40**(20), 5407–5411 (2005)
2. F. Furno, K.S. Morley, B. Wong, B.L. Sharp, P.L. Arnold, S.M. Howdle, R. Bayston, P.D. Brown, P.D. Winship, H.J. Reid, Silver nanoparticles and polymeric medical devices: a new approach to prevention of infection? *J. Antimicrob. Chemother.* **54**(6), 1019–1024 (2004)
3. M.T. Hsiao, S.F. Chen, D.B. Shieh, C.S. Yeh, One-pot synthesis of hollow Au₃Cu₁ spherical-like and biomineral botallackite Cu₂(OH)₃Cl flowerlike architectures exhibiting antimicrobial activity. *J. Phys. Chem. B* **110**(1), 205–210 (2006)
4. L. Han, C. Zhu, P. Hu, S. Dong, One-pot synthesis of a Au@TiO₂ core-shell nanocomposite and its catalytic property. *RSC Adv.* **3**(31), 12568–12570 (2013)
5. J. Di, J. Xia, Y. Ge, H. Li, H. Ji, H. Xu, Q. Zhang, H. Li, M. Li, Novel visible-light-driven CQDs/Bi₂WO₆ hybrid materials with enhanced photocatalytic activity toward organic pollutants degradation and mechanism insight. *Appl. Catal. B* **168**, 51–61 (2015)
6. X. Chen, S. Shen, L. Guo, S.S. Mao, Semiconductor-based photocatalytic hydrogen generation. *Chem. Rev.* **110**(11), 6503–6570 (2010)
7. S. Linic, P. Christopher, D.B. Ingram, Plasmonic-metal nanostructures for efficient conversion of solar to chemical energy. *Nat. Mater.* **10**(12), 911 (2011)
8. A.F. Shojaei, A. Shams-Nateri, M. Ghomashpasand, Comparative study of photocatalytic activities of magnetically separable WO₃/TiO₂/Fe₃O₄ nanocomposites and TiO₂, WO₃/TiO₂ and TiO₂/Fe₃O₄ under visible light irradiation. *Superlattices Microstruct.* **88**, 211–224 (2015)
9. Q. Zhang, I. Lee, J.B. Joo, F. Zaera, Y. Yin, Core-shell nanostructured catalysts. *Acc. Chem. Res.* **46**(8), 1816–1824 (2012)
10. R. Ghosh Chaudhuri, S. Paria, Core/shell nanoparticles: classes, properties, synthesis mechanisms, characterization, and applications. *Chem. Rev.* **112**(4), 2373–2433 (2011)
11. S. Wojtyła, T. Baran, Insight on doped ZnS and its activity towards photocatalytic removing of Cr(VI) from wastewater in the presence of organic pollutants. *Mater. Chem. Phys.* **212**, 103–112 (2018)
12. S. Wojtyła, T. Baran, Photocatalytic H₂ production over RuO₂@ZnS and RuO₂@CuS nanostructures. *Int. J. Hydrogen Energy* **44**(29), 14624–14634 (2019)
13. S. Esplugas, J. Gimenez, S. Contreras, E. Pascual, M. Rodríguez, Comparison of different advanced oxidation processes for phenol degradation. *Water Res.* **36**(4), 1034–1042 (2002)
14. E. Marais, T. Nyokong, Adsorption of 4-nitrophenol onto Amberlite® IRA-900 modified with metallophthalocyanines. *J. Hazard. Mater.* **152**(1), 293–301 (2008)
15. W.J. Sun, J. Li, G.P. Yao, M. Jiang, F.X. Zhang, Efficient photo-degradation of 4-nitrophenol by using new CuPp-TiO₂ photocatalyst under visible light irradiation. *Catal. Commun.* **16**(1), 90–93 (2011)
16. M. Panizza, G. Cerisola, Electro-Fenton degradation of synthetic dyes. *Water Res.* **43**(2), 339–344 (2009)
17. Y. Zhang, L. Wu, W. Lei, X. Xia, M. Xia, Q. Hao, Electrochemical determination of 4-nitrophenol at polycarbazole/N-doped graphene modified glassy carbon electrode. *Electrochim. Acta* **146**, 568–576 (2014)
18. Y. Du, H. Chen, R. Chen, N. Xu, Synthesis of p-aminophenol from p-nitrophenol over nano-sized nickel catalysts. *Appl. Catal. A* **277**(1–2), 259–264 (2004)
19. S. Saha, A. Pal, S. Kundu, S. Basu, T. Pal, Photochemical green synthesis of calcium-alginate-stabilized Ag and Au nanoparticles and their catalytic application to 4-nitrophenol reduction. *Langmuir* **26**(4), 2885–2893 (2009)
20. P.K. Stoimenov, R.L. Klinger, G.L. Marchin, K.J. Klabunde, Metal oxide nanoparticles as bactericidal agents. *Langmuir* **18**(17), 6679–6686 (2002)
21. S. Kim, H.J. Kim, Anti-bacterial performance of colloidal silver-treated laminate wood flooring. *Int. Biodeterior. Biodegrad.* **57**(3), 155–162 (2006)
22. P. Gong, H. Li, X. He, K. Wang, J. Hu, W. Tan, S. Zhang, X. Yang, Preparation and antibacterial activity of Fe₃O₄@Ag nanoparticles. *Nanotechnology* **18**(28), 285604 (2007)
23. M. Böswald, S. Lugauer, A. Regenfus, G.G. Braun, P. Martus, C. Geis, S. Scharf, T. Bechert, J. Greil, J.P. Guggenbichler, Reduced rates of catheter-associated infection by use of a new silver-impregnated central venous catheter. *Infection* **27**(1), S56–S60 (1999)
24. M. Pelaez, N.T. Nolan, S.C. Pillai, M.K. Seery, P. Falaras, A.G. Kontos, P.S. Dunlop, J.W. Hamilton, J.A. Byrne, K. O'shea, M.H. Entezari, A review on the visible light active titanium dioxide photocatalysts for environmental applications. *Appl. Catal. B* **125**, 331–349 (2012)
25. A.T. Babu, R. Antony, Green synthesis of silver doped nano metal oxides of zinc & copper for antibacterial properties, adsorption, catalytic hydrogenation & photodegradation of aromatics. *J. Environ. Chem. Eng.* **7**(1), 102840 (2019)
26. A. Becheri, M. Dürr, P.L. Nostro, P. Baglioni, Synthesis and characterization of zinc oxide nanoparticles: application to textiles as UV-absorbers. *J. Nanopart. Res.* **10**(4), 679–689 (2008)
27. S. Ahmad, U. Riaz, A. Kaushik, J. Alam, Soft template synthesis of super paramagnetic Fe₃O₄ nanoparticles a novel technique. *J. Inorg. Organomet. Polym. Mater.* **19**(3), 355–360 (2009)
28. X. Sun, C. Zheng, F. Zhang, Y. Yang, G. Wu, A. Yu, N. Guan, Size-controlled synthesis of magnetite (Fe₃O₄) nanoparticles coated with glucose and gluconic acid from a single Fe(III) precursor by a sucrose bifunctional hydrothermal method. *J. Phys. Chem. C* **113**(36), 16002–16008 (2009)
29. R. Georgekutty, M.K. Seery, S.C. Pillai, A highly efficient Ag-ZnO photocatalyst: synthesis, properties, and mechanism. *J. Phys. Chem. C* **112**(35), 13563–13570 (2008)
30. G. Sangeetha, S. Rajeshwari, R. Venkatesh, Green synthesis of zinc oxide nanoparticles by aloe barbadensis miller leaf extract: structure and optical properties. *Mater. Res. Bull.* **46**(12), 2560–2566 (2011)
31. H. Zeng, G. Duan, Y. Li, S. Yang, X. Xu, W. Cai, Blue luminescence of ZnO nanoparticles based on non-equilibrium processes: defect origins and emission controls. *Adv. Func. Mater.* **20**(4), 561–572 (2010)
32. S.A. Ansari, M.M. Khan, M.O. Ansari, J. Lee, M.H. Cho, Biogenic synthesis, photocatalytic, and photoelectrochemical performance of Ag-ZnO nanocomposite. *J. Phys. Chem. C* **117**(51), 27023–27030 (2013)
33. E. Romanova, A. Melnikov, Y. Kuzutkina, V. Shiryaev, S. Guizard, A. Mouskeftaras, Nonlinear optical properties of amorphous semiconductors. in *2012 International Conference on Mathematical Methods in Electromagnetic Theory* (IEEE, New Jersey, 2012), pp. 521–526
34. J. Lee, H.S. Shim, M. Lee, J.K. Song, D. Lee, Size-controlled electron transfer and photocatalytic activity of ZnO–Au nanoparticle composites. *J. Phys. Chem. Lett.* **2**(22), 2840–2845 (2011)

35. A.B. Djurišić, X. Chen, Y.H. Leung, A.M.C. Ng, ZnO nanostructures: growth, properties and applications. *J. Mater. Chem.* **22**(14), 6526–6535 (2012)
36. K. Vanheusden, W.L. Warren, C.H. Seager, D.R. Tallant, J.A. Voigt, B.E. Gnade, Mechanisms behind green photoluminescence in ZnO phosphor powders. *J. Appl. Phys.* **79**(10), 7983–7990 (1996)
37. A.B. Djurišić, Y.H. Leung, W.C. Choy, K.W. Cheah, W.K. Chan, Visible photoluminescence in ZnO tetrapod and multipod structures. *Appl. Phys. Lett.* **84**(14), 2635–2637 (2004)
38. X. Feng, H. Guo, K. Patel, H. Zhou, X. Lou, High performance, recoverable Fe₃O₄/ZnO nanoparticles for enhanced photocatalytic degradation of phenol. *Chem. Eng. J.* **244**, 327–334 (2014)
39. A. Roychowdhury, S.P. Pati, S. Kumar, D. Das, Effects of magnetite nanoparticles on optical properties of zinc sulfide in fluorescent-magnetic Fe₃O₄/ZnS nanocomposites. *Powder Technol.* **254**, 583–590 (2014)
40. A.M. Jubb, H.C. Allen, Vibrational spectroscopic characterization of hematite, maghemite, and magnetite thin films produced by vapor deposition. *ACS Appl. Mater. Interfaces* **2**(10), 2804–2812 (2010)
41. B. Mercyrani, R. Hernandez-Maya, M. Solís-López, C. Th-Th, S. Velumani, Photocatalytic degradation of Orange G using TiO₂/Fe₃O₄ nanocomposites. *J. Mater. Sci.* **29**(18), 15436–15444 (2018)
42. Z.Q. Li, H.L. Wang, L.Y. Zi, J.J. Zhang, Y.S. Zhang, Preparation and photocatalytic performance of magnetic TiO₂-Fe₃O₄/graphene (RGO) composites under VIS-light irradiation. *Ceram. Int.* **41**(9), 10634–10643 (2015)
43. Y. Lin, D. Li, J. Hu, G. Xiao, J. Wang, W. Li, X. Fu, Highly efficient photocatalytic degradation of organic pollutants by PANI-modified TiO₂ composite. *J. Phys. Chem. C* **116**(9), 5764–5772 (2012)
44. A.M. Bell, J.N.B. Smith, J.P. Attfield, J.M. Rawson, K. Shankland, W.I. David, A synchrotron X-ray powder diffraction study of 4-(2,3,4-trifluorophenyl)-1,2,3,5-dithiadiazolyl. Crystal structure determination using a global optimisation method. *New J. Chem.* **23**(6), 565–567 (1999)
45. H. Zhang, G. Chen, Potent antibacterial activities of Ag/TiO₂ nanocomposite powders synthesized by a one-pot sol-gel method. *Environ. Sci. Technol.* **43**(8), 2905–2910 (2009)
46. O. Yamamoto, Influence of particle size on the antibacterial activity of zinc oxide. *Int. J. Inorg. Mater.* **3**(7), 643–646 (2001)
47. D.K. Kim, Y. Zhang, J. Kehr, T. Klason, B. Bjelke, M. Muhammed, Characterization and MRI study of surfactant-coated superparamagnetic nanoparticles administered into the rat brain. *J. Magn. Magn. Mater.* **225**(1–2), 256–261 (2001)
48. D. Touati, Iron and oxidative stress in bacteria. *Arch. Biochem. Biophys.* **373**(1), 1–6 (2000)
49. L.E. Shi, Z.H. Li, W. Zheng, Y.F. Zhao, Y.F. Jin, Z.X. Tang, Synthesis, antibacterial activity, antibacterial mechanism and food applications of ZnO nanoparticles: a review. *Food Addit. Contam. A* **31**(2), 173–186 (2014)
50. R.K. Dutta, B.P. Nenangathu, M.K. Gangishetty, A.V.R. Reddy, Antibacterial effect of chronic exposure of low concentration ZnO nanoparticles on *E. coli*. *J. Environ. Sci. Health A* **48**(8), 871–878 (2013)
51. Y. Jiang, L. Zhang, D. Wen, Y. Ding, Role of physical and chemical interactions in the antibacterial behavior of ZnO nanoparticles against *E. coli*. *Mater. Sci. Eng. C* **69**, 1361–1366 (2016)

Publisher's Note Springer Nature remains neutral with regard to jurisdictional claims in published maps and institutional affiliations.